

RESEARCH ARTICLE | APRIL 26 2024

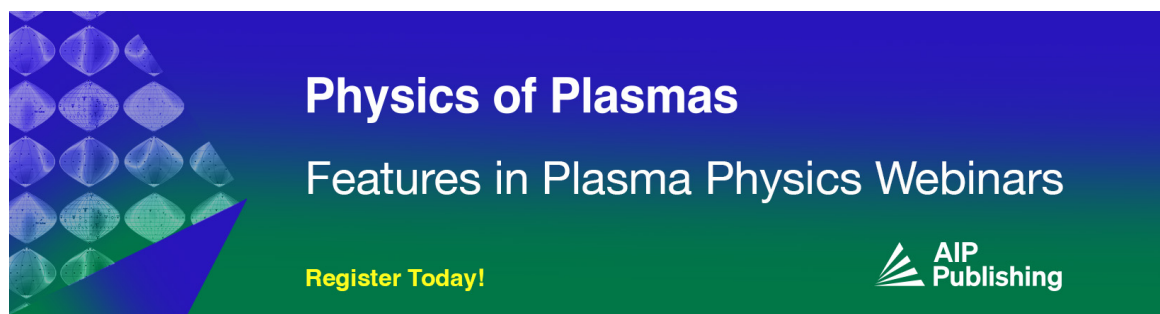
## Self-consistent charge transport model with ionization for the *alphie* plasma thruster

J. Gonzalez ; L. Conde ; J. M. Donoso 



*Phys. Plasmas* 31, 043514 (2024)

<https://doi.org/10.1063/5.0180112>



**Physics of Plasmas**  
Features in Plasma Physics Webinars

Register Today!



# Self-consistent charge transport model with ionization for the *alphie* plasma thruster

Cite as: Phys. Plasmas **31**, 043514 (2024); doi: 10.1063/5.0180112

Submitted: 7 October 2023 · Accepted: 6 April 2024 ·

Published Online: 26 April 2024



View Online



Export Citation



CrossMark

J. Gonzalez,<sup>1,a)</sup> L. Conde,<sup>2</sup> and J. M. Donoso<sup>2</sup>

## AFFILIATIONS

<sup>1</sup>Advanced Research Center for Nanolithography, Science Park 106, 1098 XG Amsterdam, The Netherlands

<sup>2</sup>Department of Applied Physics, Escuela Técnica Superior de Ingeniería Aeronáutica y del Espacio, Universidad Politécnica de Madrid, 28040 Madrid, Spain

<sup>a)</sup> Author to whom correspondence should be addressed: [j.gonzalez@arcnl.nl](mailto:j.gonzalez@arcnl.nl)

## ABSTRACT

The Alternative Low-Power Hybrid Ion Engine (*alphie*) is a new technology for space propulsion based on plasma. Its distinct characteristic is the counterflow of charges (ions and electrons) passing through its two-grid system. This means that electrons coming from an external cathode are accelerated toward the ionization chamber, in which a neutral gas (typically Ar) is injected. The strong magnetic field therein confines these electrons, which ionize and exchange energy with the propellant gas. Thus, the operation of *alphie* is strongly affected by the electrons coming from the external cathode and their collisions with the neutral atoms. This work studies the counterflow employing a particle-in-cell simulation of ions and electrons passing through a single hole as a function of the electron cathode currents ( $I_{ce}$ ) and potential drops between grids ( $V_{AC}$ ). Transparency of the grid system to ions and electrons and the ion current extracted by the grid system are studied under sweeps of these two parameters. The number of ionization events by each high-energy electron entering the ionization chamber is evaluated using a physical model based on the gas density and the cross section for ionization. These new ions are then extracted by the same electric field that accelerates the electrons inward. Thus, simulations are self-consistent, since the ionizing electron flow from the external cathode drives the ion outflow at the exit section of the two-grid system. The electrical transparency of the two-grid system to ions and electrons, related to the axial charge currents, is also studied under sweeps of aforementioned operation parameters. This new way to deal with ionizations can be useful to study other plasma thrusters in which electrons for ionization come from an external cathode without modeling the complex structure of the ionization chamber.

© 2024 Author(s). All article content, except where otherwise noted, is licensed under a Creative Commons Attribution (CC BY) license (<https://creativecommons.org/licenses/by/4.0/>). <https://doi.org/10.1063/5.0180112>

## I. INTRODUCTION

Electromagnetic plasma thrusters for propulsion in space operate like conventional chemical engines, according to the basic principle of action and reaction, where the velocity  $v_{ex}$  of the ejected gas or plasma is crucial to generate thrust. In chemical thrusters, the maximum achievable velocity of gas is limited by the energy stored per unit of propellant mass. However, this limit can be exceeded when plasma ions are accelerated by electromagnetic fields.<sup>1,2</sup>

Typical ion exhaust velocities from plasma thrusters are  $\sim 10 - 40$  km/s, one to two orders of magnitude higher than those of gases ejected by chemical engines, providing higher specific impulses  $I_{sp} = v_{ex}/g_0$ , where  $g_0$  is the standard acceleration of the Earth. However, the rate of ion mass production  $\dot{m}_i$  is usually small, as it is limited by the reduced electrical power available in spacecraft. Therefore, plasma thrusters are characterized by the low thrust  $T = \dot{m}_i v_{ex}$  delivered and high specific impulses. These features are advantageous for

certain orbital maneuverers, such as station keeping, flight formation, and/or end-of-life removal of Earth-orbiting satellites.<sup>2,3</sup>

Conventional gridded ion engines (GIEs) extract a current of ions from a plasma that are accelerated in the steady electric field produced by a set of grids connected to high voltages, called the *ion optic system*. An ejected plasma beam (called *plasma plume*) is formed when exiting ions are neutralized by a flow of free electrons from an external cathode.<sup>1,2</sup> In this conventional GIE scheme, plasma production and ion acceleration are separate processes, and, thus, transport of ions through the grids is limited by space-charge effects.<sup>1,4</sup> The maximum ion current scales according to the Child-Langmuir law for plane electrodes.<sup>1,5</sup> Recently, corrections introduced by the divergence of the ion beam in three dimensions have been considered.<sup>4</sup>

In Hall effect thrusters (HETs)<sup>1-3</sup> and multi-cusp field thrusters (MCFTs), such as the HEMPT (*highly efficient multistage plasma thruster*),<sup>6,7</sup> the ions are created by a plasma discharge inside cylindrical

and/or the annular ionization chambers. Different magnetic field configurations confine the ionizing electrons provided by an external cathode, and a self-consistent electric field develops in the plasma, accelerating the ions up to supersonic velocities. In these thrusters, the collisional ionization of propellant gas is closely connected with the acceleration of positive charges, and the ion beam current is not space-charge limited.

The Alternative Low-Power Hybrid Ion Engine (*alphie*)<sup>8,9</sup> is a gridded plasma thruster different to the classical GIE configuration, which can be categorized as a *hybrid* concept.<sup>10,11</sup> Fast electrons from an external cathode reach the ionization chamber, accelerated by the system of two grids that simultaneously extract the ions in the opposite direction. These high-energy electrons, trapped by the magnetic field inside the ionization chamber, collide with the propellant gas, which is partially ionized. This is a distinct characteristic of the *alphie* thruster: ions and ionizing electrons from the cathode counterflow through the open spaces of the grids in opposite directions. Similarly to HET and MCFT thrusters, in the *alphie*, the propellant ionization and the acceleration of charged particles are connected processes.

In all electric propulsion systems, focusing of the ion beam, achieving maximum ion flow along its axial direction, and maximizing the momentum transfer to the vehicle have an important impact on efficiency. However, the existence of a radial electric field can increase the divergence of the ion beam, reducing its efficiency and increasing the possible contamination of the vessel. Numerical simulations allow analyzing the plasma plume dynamics for different configurations of a given thruster, saving expensive laboratory testing. The study of the electric charge flow in the *alphie*, HETs, and MCFTs requires an ion and electron plasma model, whereas in conventional GIEs, only the motion of ions through the grids is considered.

Plasma models are employed when it is necessary to simultaneously consider the motions of electrons and ions as well as elementary processes between charged species and neutral atoms, such as excitation, ionizing electron collisions, charge-exchange, etc. Particle-in-cell (PIC) simulations have been employed to study HETs,<sup>12</sup> MCFT,<sup>13,14</sup> HEMPT,<sup>15</sup> and the *alphie*<sup>16,17</sup> thrusters.

The ion extraction analysis demands a representation of the thruster's basic components that connect the laboratory operation parameters with the spatial profile of positive charge outflow, which delivers the impulse. The *alphie* plasma thruster consists of the propellant gas flow, the influx of ionizing electrons from its external cathode, and the acceleration potential that controls the throttle. In this paper, we improve previous PIC simulations using the *fpac* (Finite element Particle Kinetic Code) code<sup>16,17</sup> together with a model that consistently relates the above operating parameters to the space profiles of density and velocity of the ions at the exit section of the *alphie* thruster. As the energy distribution of electrons is significant for the ionization process in *alphie*, both species, ions and electrons, have to be simulated with a kinetic approach.

Additionally, these fully kinetic PIC simulations allow us to study the process of charge acceleration by the steady self-consistent electric field created in the open space of *alphie's* grid system by the counterflow of ions and electrons and the voltages applied to the grids. The number of charges captured by the grids at a fixed geometry and per voltage assigned to the grids can be then estimated. The transparency of the system, i.e., the ratio of current before and after the grids, is defined then by the geometry of the grids, *geometrical*

*transparency*, and by the electric field formed between them, *electrical transparency*.

This simplified model for the propellant gas ionization process is not exclusive to the *alphie* thruster and can be extended to above-mentioned other concepts, such as HETs, MCFTs, or HEMPTs, where the ion transport is closely connected with collisional gas ionization.

This work is organized as follows. Section II presents an overview of the typical operation of the thruster for easy reading of this work, and Sec. III contains an overview of the numerical code employed. The computational model employed for the simulations, including the model to account for the gas ionization, is described in Sec. IV. Results for the different operational parameters of the *alphie* thruster are presented in Sec. V. Finally, conclusions are given in Sec. VI.

## II. THE OPERATION OF THE ALPHIE PLASMA THRUSTER

The *alphie* plasma thruster is a new kind of ion engine that uses only one external cathode placed in front of its two-grid system for both the ionization of propellant gas and ion beam neutralization. Its operation has been covered in the past,<sup>8,9,18,19</sup> and it is briefly summarized in this section for a better understanding of present numerical simulations.

The schematic diagram in Fig. 1 shows its longitudinal cross section together with its electrical connections. The two flat parallel grids of the *alphie* plasma thruster are represented in Fig. 1 by vertical dashed lines. The *ion extraction* grid is negatively polarized by the  $-V_{EG}$  voltage regarding the metallic walls of the ionization chamber, and the potential  $-V_{AC} - V_{CG}$  is applied to the *cover* grid. Since  $V_{EG} \ll V_{AC} + V_{CG}$ , an electric field develops between both grids that accelerates the ions outward the ionization chamber and the electrons inward. The external cathode is connected to the  $-V_{CG}$  potential regarding the cover grid, which is set to null in normal operation, so that the cover grid and the electron source are electrically connected.

When the cathode is heated up to the thermionic electron emission by the electric power  $P_W = V_{CH}I_{CH}$ , a fraction of emitted electrons flow through the aligned holes of the cover and extraction grids,

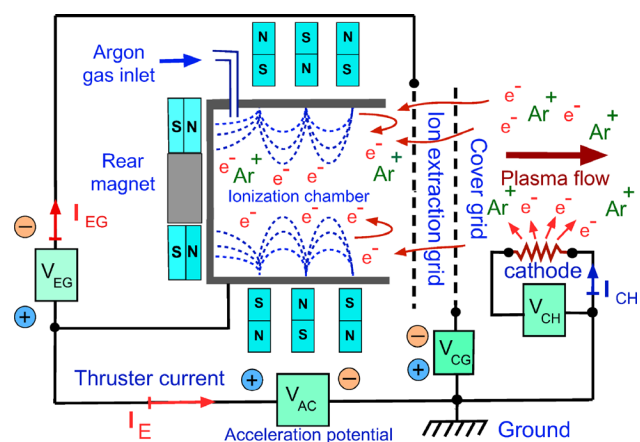


FIG. 1. Electrical scheme of *alphie* plasma thruster, where a single external cathode provides the electrons for ion beam neutralization and neutral gas ionization inside the chamber. In the two-grid system, a counterflow of ions and electrons appears in the steady operation regime. Figure modified from Ref. 9.

spaced 2 mm apart. These electrons are accelerated toward the ionization chamber of 10 cm in length and 4 cm in diameter. They are confined along the magnetic field lines indicated by the dotted lines in Fig. 1, produced by a set of permanent magnets, causing the collisional ionization of the argon gas used as propellant. The motion of heavy Ar<sup>+</sup> ions is essentially unaffected by this magnetic field and moves toward the extraction grid, and a fraction is accelerated outward by the electric field established between the grids.

In the steady state, high-energy electrons from the cathode and secondaries from the ionization events are trapped by the magnetic field inside the ionization chamber. A high-speed population of ions is accelerated outward, and also ionizing electrons from the cathode move inward through the holes of the two-grid system of the *alphie* plasma thruster.

A self-consistent electric field is established in the open spaces of the grids by the currents of cathode electrons, ions, and the electric potentials applied to the grids. The grids are considered as equipotential surfaces because the size of their open spaces is below the characteristic electron Debye length. The *thruster-current*  $I_E$  in Fig. 1 characterizes this counterflow of charges with opposite signs, which constitutes a crucial difference from conventional ion engines, in which only a current of ions is transported through its ion optic system. This means that *alphie's* grids system is not limited by the Child-Langmuir law.<sup>4,20</sup>

In direct measurements of thrust,<sup>8,9</sup> the *alphie* prototypes deliver impulses in the mN range for argon gas flows below 1 sccm, and this gives specific impulses on the order of  $I_{sp} \sim 10^4$  s. This is higher than the specific impulse achieved only by the ion velocities measured ( $I_{sp} = V_{ex}/g$ ), meaning that the un-ionized propellant could have a significant impact in thrust generation. The axial profile of electron and ion populations in the plasma plume has also been characterized in the laboratory.<sup>8,9</sup> The plasma densities are much lower than those required for the amplification of disturbances associated with charge transport, such as the two-stream instability.<sup>21</sup>

However, measurements inside the ionization chamber and in the space between grids are extremely difficult to carry out. Consequently, numerical simulations have to be employed to better understand the charges' dynamics in these regions. Specifically, the local self-consistent electric field and the charged particle transport through the open spaces of the two grids. The *thruster-current*  $I_E$  can be numerically studied using the electron and ion current per hole of the two-grid system, as in Refs. 16 and 22. A self-consistent numerical simulation requires relating the ionizing electron flow coming from the external cathode in Fig. 1 with the outflow of ions.

### III. THE PARTICLE-IN-CELL CODE FPAKC

The dynamics of the electrons and ions currents through the two-grids system in the *alphie* thruster is studied using a fully kinetic explicit particle-in-cell (PIC) code named *fpakc* (Finite element PArticle Kinetic Code). Its unstructured finite-element mesh tool has been used before to study the grids' performance under variations of geometrical parameters of its two-grid system.<sup>17</sup>

In PIC codes, numerous macro-particles, representing an even larger amount of physical particles, are used to simulate the dynamics of the different plasma species. The macro-particles have the same charge-to-mass ratio as the actual particle they substitute, and the relation between the number physical of particles and macro-particles is

usually called the *specific weight*. This value is assigned for each individual particle species in the *fpakc* input file.

The equations of motion for each macro-particle,

$$\frac{d\mathbf{v}_\alpha}{dt} = \frac{q_\alpha}{m_\alpha} (\mathbf{E} + \mathbf{v}_\alpha \times \mathbf{B}), \quad (1)$$

$$\frac{d\mathbf{r}_\alpha}{dt} = \mathbf{v}_\alpha, \quad (2)$$

are numerically solved in cylindrical symmetry, where  $\mathbf{r} = (r, z)$ ,  $\mathbf{v} = (v_r, v_z, v_\theta)$ , and  $\mathbf{E}$  and  $\mathbf{B}$  are the electric and magnetic fields, respectively. Particles are advanced in time with a leapfrog second-order scheme in a mesh composed of first-order finite elements. As Fig. 2 shows, the speed  $v_z$  is the component of the velocity along the axis of symmetry of the two-grid system and  $v_r$  the perpendicular radial component. Under the assumption of cylindrical symmetry, the angular momentum  $L_z \sim r v_\theta$  is conserved in the simulation. Equations (1) and (2) are made dimensionless using the characteristic electron Debye length  $\lambda_{De}$ , the plasma electron frequency  $f_{pe}$ , and the electron thermal speed.

PIC codes cyclically perform four actions at each computational iteration, namely, *particle push*, *charge deposition*, *field solver*, and, finally, *particle gather*. In the first, the *push step*, the equations of motion for each particle are solved in cylindrical symmetry. The unphysical singularity for  $r \rightarrow 0$  in the computational domain of Fig. 2 is avoided by using a Boris mover<sup>23,24</sup> that calculates the particle velocity in Cartesian coordinates that are later transferred into its cylindrical components.

The following *charge deposition* step is crucial in PIC codes, since it relates the particle distribution with the self-consistent electric field. The local charge density is determined by linear interpolation at the vertices of the simulation cell wherein each macro-particle is found at the end of the *push step*.

In the next *field solver* stage, the new electric field  $\mathbf{E} = -\nabla\phi$  in Eq. (1) is calculated as the numerical solutions of Poisson's equation,

$$\nabla^2\phi = -\frac{1}{\epsilon_0} \sum_\alpha q_\alpha n_\alpha, \quad (3)$$

in cylindrical coordinates  $(z, r)$  within the discretized domain of Fig. 2. Here,  $\phi$  is the electric potential,  $\epsilon_0$  is the vacuum permittivity, and  $n_\alpha$

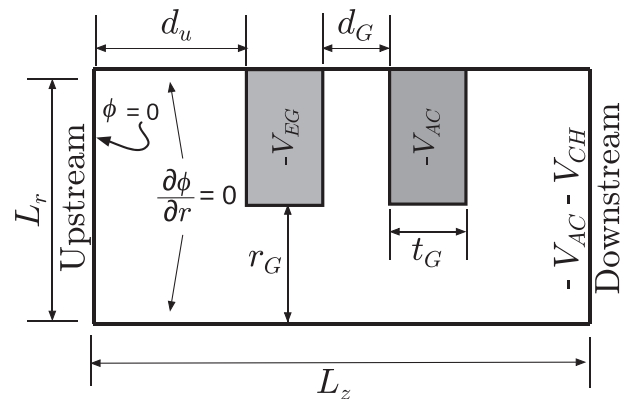


FIG. 2. The numerical domain of two-grid *alphie* thruster system with its boundary conditions where  $d_g$  is the distance between both meshes and  $t_G$  is the grid thickness. The cover grid voltage  $V_{CG}$  is assumed to be 0.

is the charged particle densities calculated in the previous *push* step. This equation is solved in the finite-element mesh based on the LU decomposition method provided in OpenBLAS,<sup>25</sup> which *fpac* uses to track the particles considering the shape of the element, the charge density at the nodes and the boundary conditions at the edges. As it is typical in finite element methods, the stiffness matrix of the system is build based on the elements, and the load vector is composed of the charge density and Dirlecht boundary conditions for the electric potential.

In the final *particle gather* step, the axial and radial electric fields applied to each macro-particle are calculated by linear interpolation of the field evaluated at the vertices defining the cell in which the particle is located. This step closes the recursive cycle of our PIC code mentioned earlier that continues performing a new *push* stage.

#### IV. THE COMPUTATIONAL MODEL

In the *alphie* prototype, the *cover* and *extraction* grids of Fig. 1 have 665 aligned holes arranged in a rectangular pattern. The actual physical dimensions of the *alphie* two-grid system and other relevant parameters employed in our simulations are presented in Table I.

The region close to two aligned central holes is translated into the computational domain of Fig. 2, where  $z \in [0, L_z]$ ,  $r \in [0, L_r]$ , and axial symmetry is assumed. The *alphie* ionization chamber is located upstream of the ion flow, at the left in Fig. 2, whereas the only electron-emitting cathode is located downstream of the ion beam exhaust. The radius of the holes is  $r_G$ , and the grids of thickness  $t_G$  are separated by the distance  $d_g$ .

As shown in Fig. 2, the upstream electric potential, located at a distance  $d_u$  from the ion extraction grid, is set to null  $\phi(r, 0) = 0$ . The plasma potential inside the ionization chamber is assumed to be equal to the potential of the upstream side, meaning that no additional acceleration is assumed for the electrons in the ionization chamber. The grids are set to the corresponding voltages presented in Table I. The radial components  $E_r \simeq -\partial\phi/\partial r$  are also null at the top and bottom boundaries of the computational domain, as indicated in Fig. 2. This is required to match the reflection boundary condition set to the particles to represent the effect of neighbor holes and to fulfill the condition of axis-symmetry at  $r = 0$ . The voltage at the downstream region is fixed to a voltage lower than  $V_{AC}$  to avoid the formation of a sheath as the density of electron increases.

TABLE I. Characteristic parameters of the *alphie* grid system and the operation voltages applied to its acceleration and extraction grids.<sup>8,9</sup>

Name, units	Symbol	Value
Axial length, mm	$L_z$	10.0
Radial length, mm	$L_r$	0.6
Grid hole, mm	$r_G$	0.5
Grid thickness, mm	$t_G$	0.5
Distance between grids, mm	$d_G$	2.0
Upstream distance, mm	$d_u$	2.0
Extraction grid voltage, V	$V_{EG}$	150
Acceleration grid voltage, V	$V_{AC}$	[400,600]
Downstream voltage, V	$V_{CH}$	100

The plasma parameters in this study are suggested by laboratory experiments.<sup>18,26</sup> The typical thruster currents in the experiments<sup>18</sup> of  $I_E \simeq 100\text{--}500$  mA give a current per hole of  $I_h = I_E/665 \sim 0.15\text{--}0.75$  mA transported through the computational domain of Fig. 2. In this current  $I_h = I_{hi} + I_{he}$ , the contribution of ions  $I_{hi}$  is orders of magnitude much lower than the electron current  $I_{he} \gg I_{hi}$  and similar to the flow per hole of ionizing electrons  $I_{ce} \simeq I_{he}$  from the cathode, placed at the downstream side of Fig. 2. The azimuthal magnetic field produced by this low current can be neglected as well as the motion of charged particles perpendicular to the plane of Fig. 2. From the data presented in Sec. V, the electron density current,  $J_e$ , in the grid hole can be estimated as  $1.27 \times 10^3$  A m<sup>-2</sup>, which results in a magnetic field given by  $B = \frac{\mu_0 r_G J_e}{2}$ , where  $\mu_0$  is the vacuum permeability, of  $10^{-7}$  T, which has no impact on the ions or electrons trajectories.

For the plasma plume, the typical electron densities are of  $n_e \simeq 4 \times 10^{14}$  m<sup>-3</sup> and the electron temperatures of  $T_e \sim 1\text{--}2$  eV. These give a typical Debye length  $\lambda_{De} \in [0.4, 0.5]$  mm, electron  $f_{pe} \sim 180$  MHz, and ion  $f_{pi} \sim 0.66$  MHz plasma frequencies. Higher electron densities are expected inside the ionization chamber due to secondary electrons produced by electron impact ionization of the neutral gas, which remain inside repelled by the negative potential  $V_{EG}$  of the extraction grid.

The domain of Fig. 2 is divided in square cells with  $0.1$  mm  $\ll \lambda_{De}$  side length. The mesh is composed of 100 and 6 elements in the axial and radial positions, respectively. The specific weight, *i.e.*, the ratio of real particles to macro-particles in the simulations, is set to 10 for electrons and ions, which results in  $\sim 10^5$  macro-particles inside the numerical domain. A macro-particle abandons the simulation if it hits the grid surfaces, its coordinate  $z$  is negative, or when  $z > L_z$  exceeds the axial length of the computational domain. When a macro-particle escapes at a radial position  $r > L_r$ , its velocity is reflected to simulate the effect of neighbor grid holes.

The capability in *fpac* code to use different time steps allows to reduce the required computational time while keeping the same overall solution.<sup>22</sup> The time steps for these simulations are  $\tau_i = 10^{-9}$  s  $< f_{pi}^{-1}$  and  $\tau_e = 5 \cdot 10^{-12}$  s  $< f_{pe}^{-1}$  for argon ions and electrons, respectively. A physical time of  $7.5$   $\mu$ s is simulated for each case, which ensures that the spatial distribution of ions and electrons has reached a quasi-steady state.

#### A. A self-consistent model for ion production

The realistic simulation of ion and electron transport through the two-grids system of the *alphie* thruster requires connecting the flow of ionizing electrons from the external cathode with the production of ions within the ionization chamber. These ions enter the upstream side of Fig. 2 and, after being accelerated by the two-grid system, exit at the opposite side.

In the steady state, ions originate within the ionization chamber of Fig. 1 by the flow of ionizing electrons that enter the two-grid system from the cathode, placed on the right side. The ion production rate inside the small ionization chamber by a low energy secondary electrons can be neglected.

The model presented later allows us to relate the current  $I_{ce}$  delivered by the cathode at the downstream side of Fig. 2 with the ion production at the upstream side. Thus, the *fpac* code can self-consistently

simulate the counterflow of positive and negative charges through the two-grid system.

The electron current per hole  $I_{ce}$  delivered by the cathode of Fig. 1 determines the input electron density  $n_e$  at the downstream boundary of the two-grid system. In these simulations, this population of electrons has a temperature of 1 eV and a drift velocity of  $u_e = -4.2 \times 10^3 \text{ km s}^{-1}$ . Considering the downstream electron density  $n_e = 4 \times 10^{14} \text{ m}^{-3}$  estimated from the experiments, the resulting cathode current per hole is  $I_{ce} = 0.30 \text{ mA}$ , and the midpoint in the cathode current sweep presented in Sec. V A. Using the equation,

$$n_e = \frac{I_{ce}}{e \pi L_r^2 u_e}, \quad (4)$$

and assuming the same drift velocity of electrons for the 0.10 and 0.60 mA cathode currents, the downstream electron density increases proportionally to the current. These conditions for injection plus the fixed downstream potential allow us to study the effect of different electron populations downstream of the grid system without the formation of a sheath, reducing the electron current going toward the grid system.

The characteristic lengths ( $L_r, L_z$ ) of the two-grid system are much smaller than all collisional mean free paths for electrons. Thus, a fraction of cathode electrons located downstream side of Fig. 2 moves toward the ionization chamber of Fig. 1. Because of the high voltages involved, these electrons have enough energy to produce multiple ionizing collisions, and the number of possible events  $N_{ion}$  per electron that reaches the left side of Fig. 2 is

$$N_{ion} = \left\lfloor \frac{E_k}{I_1} \right\rfloor, \quad (5)$$

where  $\lfloor \cdot \rfloor$  is the floor function,  $E_k$  is the electron kinetic energy in a frame where the background neutral gas is at rest, and  $I_1$  is its first ionization energy of the gas. The probability of each ionizing collision  $P_{ion}$  can be computed as<sup>27,28</sup>

$$P_{ion} = 1 - \exp\left(-n_o \sigma_{ion}^{eo}(E_k) v_{rel} \frac{t_{ion}}{N_{ion}}\right), \quad (6)$$

in which  $\sigma_{ion}^{eo}(E_k)$  is the effective electron impact cross section for the first ionization energy. The neutral particle density is in Eq. (6)  $n_o$  within the ionization chamber, and it is estimated assuming the sonic expansion of the argon gas injected as

$$n_o = \frac{\Gamma_o}{cS}, \quad (7)$$

where  $\Gamma_o$  is the flow of neutrals,  $S$  is the cross section of the ionization chamber, and  $c$  is the argon gas sound speed at room temperature.

The *effective ionization time*  $t_{ion}$  in Eq. (6) refers to the residence time of fully magnetized cathode electrons trapped in the magnetic field inside the ionization chamber. This time is divided between the maximum number of effective collisions to represent an average distribution of the total residence time of the electron among the possible collisions. Thus, this time has to properly represent the average lifetime of an electron while traveling the magnetic field lines of the ionization chamber.

For the calculation of a new ion-electron pair, the following process is repeated  $N_{ion}$  times. Equation (6) is evaluated, and a random

number  $0 \leq R_a \leq 1$  is generated. If  $R_a < P_{ion}$ , an ionization event occurs, and a new pair of ion-electron macro-particles is introduced in the simulation with the same weight as the incoming electron. A random position along the edge in which the ionizing boundary condition is applied is calculated to distribute the new particles. The ion velocity is sampled from the neutral distribution, and for the secondary electron, it is assumed that it gains the ionization energy  $I_1$  and a random velocity following a Maxwellian distribution.

The kinetic energy of the incoming electron is reduced by  $E_{rel} - I_1$  after a successful ionization. This has an impact on  $P_{ion}$  for the next ionization event, increasing accuracy to avoid over-estimating the number of collision events per electron. The ionizing electron is always removed from the simulation, as it is assumed to be collected by the metallic walls of the ionization chamber.

The ions and secondary electrons produced along  $t_{ion}$  are introduced in the numerical simulation in a single time step  $\tau_e \ll t_{ion}$  related to the electron plasma frequency in the ionization process. Though this approach introduces a small deviation, it is small for quasi-steady state scenarios studied in present simulations.

## V. NUMERICAL RESULTS

The counterflow of electric charges through the two-grid system of the *alphie* plasma thruster is studied using its two characteristic operation parameters: the influx of cathode electrons  $I_{ce}$  and the  $V_{AC}$  acceleration voltage.

In the first place, three cathode currents  $I_{ce} = 0.10, 0.30,$  and  $0.60 \text{ mA}$  are simulated at the fixed  $V_{AC} = 500 \text{ V}$  voltage. These calculations will provide information on how the influx of electrons into the ionization chamber increases the exhausted ion current. Next, the acceleration voltage is modified to 400 and 600 V at the constant cathode current per hole of  $I_{ce} = 0.30 \text{ mA}$  to assess its effect on the distribution of charges upstream and downstream of the simulation domain.

In addition, the efficiency of ion and electron transport can be reduced by increments in the self-consistent electric field, governed by the  $V_{AC}$  voltage, as charges of both signs can be lost at the grids. Hence, the axial electron  $I^e$  and ion  $I^i$  currents transported through the two-grid system are studied for the two main parameters  $I_{ce}$  and  $V_{AC}$  to characterize the *electrical transparency* of the grids.<sup>29</sup>

In these numerical simulations, the neutral gas density is set to  $n_o = 10^{18} \text{ m}^{-3}$  by Eq. (7) assuming a sonic expansion at room temperature of a 1 sccm argon into the cylindrical ionization chamber of 20 mm in radius. The first energy threshold for the ionization of argon is 15.76 eV, and the electron impact ionization cross sections were obtained from Matboltz version 7.1.<sup>30,31</sup> The effective ionization time in Eq. (6) is calculated assuming the magnetic field lines configuration shown in Fig. 1 and that cathode electrons enter parallel regarding the field lines. The average velocity of electrons entering the ionization chamber is related to a potential difference of 600 V,  $\sim 15\,000 \text{ km s}^{-1}$ , equivalent to that shown in Fig. 9. It is also assumed that these electrons follow the magnetic field lines along the length of the ionization chamber ( $\sim 15 \text{ cm}$ ).<sup>8</sup> Thus, we can establish  $t_{ion} \sim 10^{-8} \text{ s}$  as the average time an electron will travel inside the ionization time as a conservative value that puts us close to the worst-case scenario. A values half and double  $t_{ion}$  have been tested without finding any significant differences in the results presented here.

The results presented in this section are time-averages between 5 and  $7.5 \mu\text{s}$  in which the plasma is in a quasi-steady state.

### A. Effects of the ionizing electron influx

The performance of the *alphie* thruster is directly related to the influx  $I_{ce}$  of ionizing electrons from the external cathode. Figure 3 shows the  $n_d^i$  radial density profiles of  $\text{Ar}^+$  downstream of the two-grids system at the exit section located at  $z = 7.5$  mm in Fig. 2. The  $\text{Ar}^+$  density for  $r \geq 0$  increases with the current of cathode electrons  $I_{ce}$  as it increases the ion production rate in the ionization chamber. Since the acceleration voltage is constant, the increment in Fig. 3 is not associated with neither ion focusing nor changes in the electric transparency of the two-grid system. Thus, the ions are contributing to the extracted current with basically the same axial velocity, as shown in Fig. 4(a), but in a higher number density due to the increased ionization events.

The current  $I_{ce}$  also has an impact on the velocity distributions of  $\text{Ar}^+$  in Fig. 4, which are represented the axial  $u_{z,d}^i$  and radial  $u_{r,d}^i$  components of the ion speed also at the  $z = 7.5$  mm downstream section. The axial acceleration imparted to ions by the two-grid system is evidenced by the difference of three orders of magnitude between their axial and radial velocities. At the edge of the domain, the  $\text{Ar}^+$  axial velocity drops abruptly, since most of the ions are focused on the hole region ( $r < 0.5$  mm) of Fig. 3.

In Fig. 4(a), the axial ion speed shows a slight increase with the ionizing electron current  $I_{ce}$  because the presence of additional electrons increases the self-consistent axial electric field between the grids. The radial velocity of  $\text{Ar}^+$  in Fig. 4(b) becomes more negative, meaning a more focused plasma beam as  $u_{z,d}^i/|u_{r,d}^i| > 100$ . That is, the increase in electron inflow shifts the axial velocity positively and the radial velocity negatively. The sharp drop in axial velocity is related to the lack of ions found in that region due to the significant collimation of the ion beam.

The *over-focusing effect*<sup>29</sup> which would spread ions at the exit section is not observed in these simulations. Consequently, the thruster plasma plume can be regarded as the superposition of 665 individual plasma beams, one per grid hole, that will combine downstream the grids system.

Finally, the ionizing electron densities at the upstream section at  $z = 1.0$  mm of the two-grid system are depicted in Fig. 5 for the three  $I_{ce}$  cathode currents. These radial electron density profiles  $n_u^e$  show that electrons are focused into the ionization chamber for  $r < 0.3$  mm and also that a higher influx of cathode electrons  $I_{ce}$  increases the upstream flux of high-energy electrons.

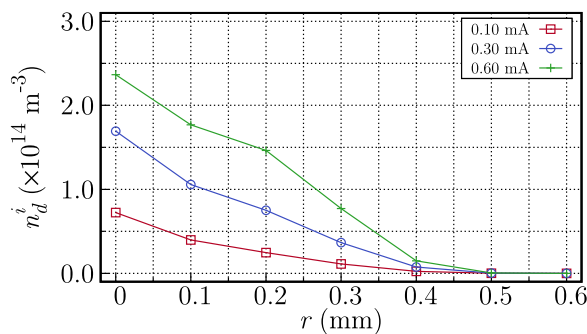
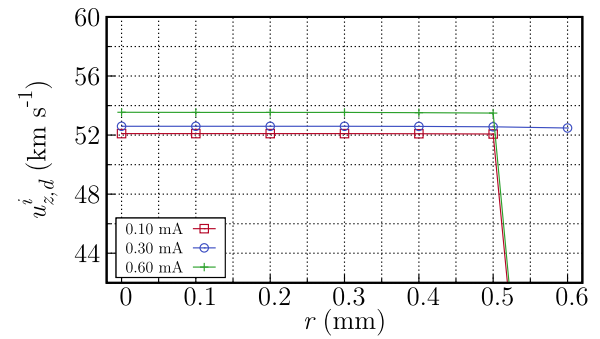
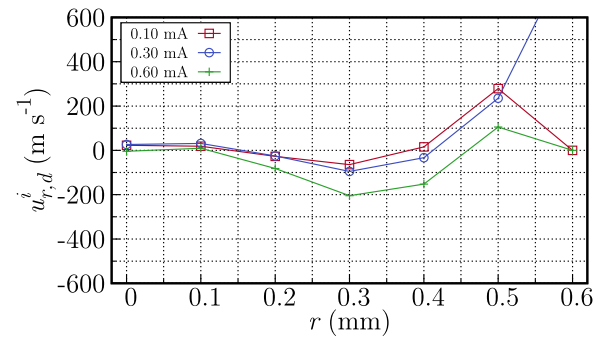


FIG. 3. Downstream ( $z = 7.5$  mm)  $\text{Ar}^+$  densities at  $V_{AC} = 500$  V for three values of electron cathode current  $I_{ce}$ . Increasing this ionizing electron current significantly increments in the ion current at the downstream side of Fig. 2.



(a)  $\text{Ar}^+$  axial velocity



(b)  $\text{Ar}^+$  radial velocity

FIG. 4. Downstream ( $z = 7.5$  mm)  $\text{Ar}^+$  axial (a) and radial (b) velocities at  $V_{AC} = 500$  V for three values of electron current from the external cathode  $I_{ce}$ . The additional cathode electrons produce a slight increase in the axial ion velocity and beam focusing. The axial ion velocity drops at the edge of the simulation domain as most ions are focused on the  $r < 0.5$  mm region. The drop in ion velocity at the edge is directly related to the collimation of the edge and lack of ions in that area.

The increase in downstream  $\text{Ar}^+$  densities in Fig. 3 and the increase in the ionizing electron densities upstream in Fig. 5 are not linear with  $I_{ce}$ , meaning that other factors, such as the grid geometry or the acceleration voltage  $V_{AC}$ , are involved in the electric charge transport through the computational domain of Fig. 2.

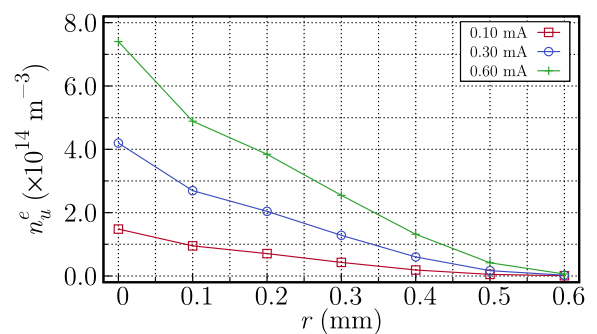


FIG. 5. Upstream ( $z = 1.0$  mm) electron density at  $V_{AC} = 500$  V for three values of  $I_{ce}$ . Increasing this current at the downstream side of Fig. 2 increments the amount of high-energy electrons reaching the ionization chamber.

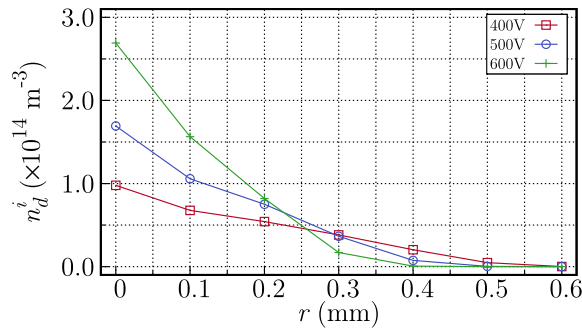


FIG. 6. Downstream ( $z = 7.5$  mm)  $\text{Ar}^+$  density for  $I_{ce} = 0.30$  mA and the acceleration voltages of 400, 500, and 600 V. Two main effects can be observed: the increase in ion density with  $V_{AC}$  and the collimation of exhausted ions.

**B. Effect of the acceleration voltage**

The experimental measurements of the *alphie* plasma plume have revealed a direct relation between the  $V_{AC}$  acceleration potential and the velocities of exhausted ion populations.<sup>8</sup> Figure 6 shows the radial profiles of  $\text{Ar}^+$  densities for  $V_{AC} = 400, 500,$  and  $600$  V at the  $z = 7.5$  mm downstream section of the computational domain. The electron cathode current  $I_{ce} = 0.30$  mA was held constant in this case.

The downstream  $\text{Ar}^+$  densities grow with  $V_{AC}$  due to two main factors: the higher energy of cathode electrons in the ionization chamber and the improved electric transparency of the two-grid system. The production of charged particles increases, and the radial ion density profiles become narrower in Fig. 6 as the acceleration potential is increased.

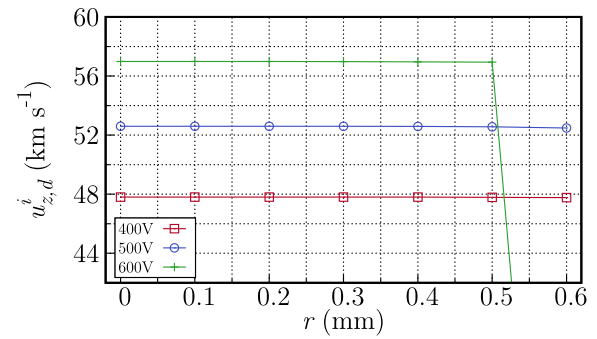
Figure 7 represents the profiles of the axial  $u_{z,d}^i$  and radial  $u_{r,d}^i$  components of the  $\text{Ar}^+$  velocity at the  $z = 7.5$  mm downstream section. Increments in the acceleration voltage are directly linked to the ion axial velocity, as shown in Fig. 7(a), and are essentially uniform along the radial direction of the computational domain.

The radial velocity component in Fig. 7(b) becomes more negative as  $V_{AC}$  increases, which indicates a better focusing of the ion beam. Hence, increments in the acceleration voltage focus the exhausted  $\text{Ar}^+$  beam. This increases the electrical transparency of the *alphie* two-grid system. A similar effect was observed in the ion optic system of conventional ion engines, in which only one species is transported through the grids' holes.<sup>32</sup>

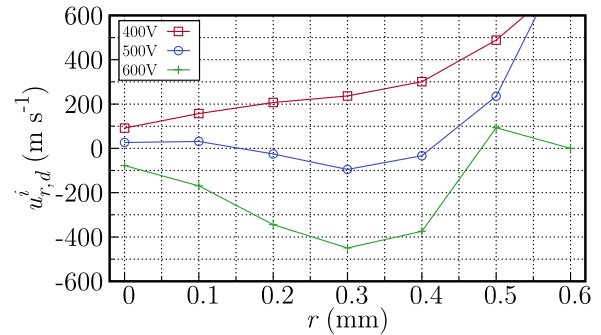
Figure 8 shows the acceleration voltage  $V_{AC}$  has also a focusing effect on the upstream electron densities, similar to that for downstream ions in Fig. 6. The electron densities at  $z = 1.0$  mm increase with the acceleration voltage, and their radial profiles become more confined. The kinetic energy of cathode electrons at the ionization chamber also increases with  $V_{AC}$  as shown in Fig. 9, which is depicted their axial velocity component. The electron velocity is directly related to the acceleration voltage, which influences the production of ions and the total current, as it will be shown in Sec. V C.

**C. The electron and ion axial currents**

The aforementioned described counterflow of ions and electrons through the grids constitutes a unique characteristic of the *alphie* thruster operation. This feature contrasts with conventional ion engines, where only ions are transported through its ion optic system.



(a)  $\text{Ar}^+$  axial velocity



(b)  $\text{Ar}^+$  radial velocity

FIG. 7. Downstream ( $z = 7.5$  mm)  $\text{Ar}^+$  axial (a) and radial (b) velocities at fixed  $I_{ce} = 0.30$  mA and the acceleration voltages of 400, 500, and 600 V. This voltage has a direct impact on the ion velocity resulting in a more focused and faster ion beam. The drop in ion velocity at the edge is directly related to the collimation of the edge and lack of ions in that area.

Thus, it is important to analyze the effect of the influx of electrons in combination with  $V_{AC}$ . Three additional  $I_{ce}$  values of 0.20, 0.40, and 0.50 mA are used for some figures in this section to better represent the performance trend of *alphie* in relation with  $I_{ce}$ .

Figure 10 shows the axial currents  $I^i$  of ions and electrons  $I^e$  flowing through the grid system for the parameter space of cathode electron currents  $I_{ce}$  and acceleration potentials  $V_{AC}$  of present numerical

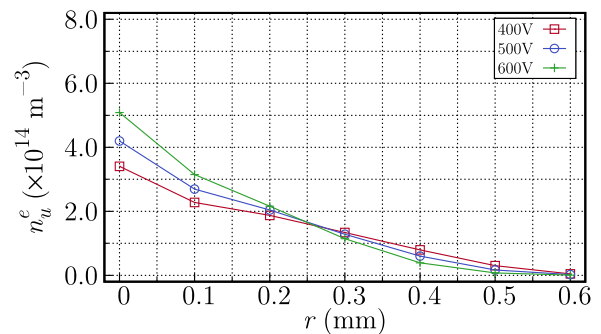
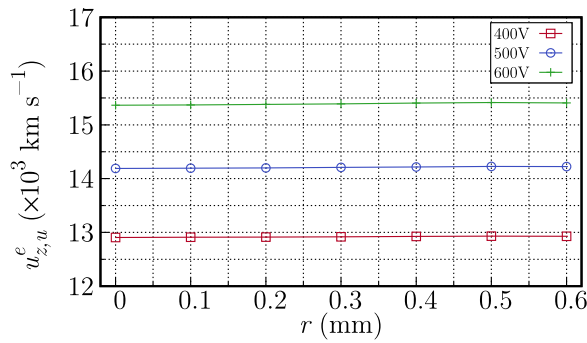


FIG. 8. Upstream ( $z = 1.0$  mm) electron density for  $I_{ce} = 0.30$  mA and the acceleration voltages of 400, 500, and 600 V. This voltage increases the electron density, and their radial distributions becomes narrower.

17 June 2024 09:36:55

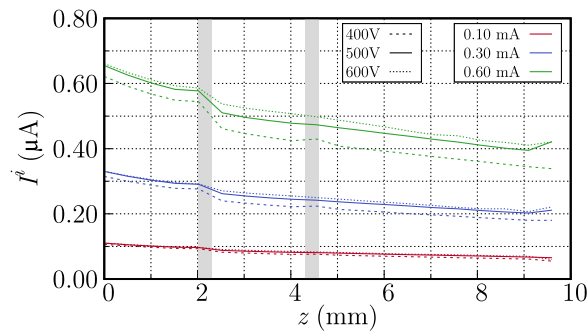




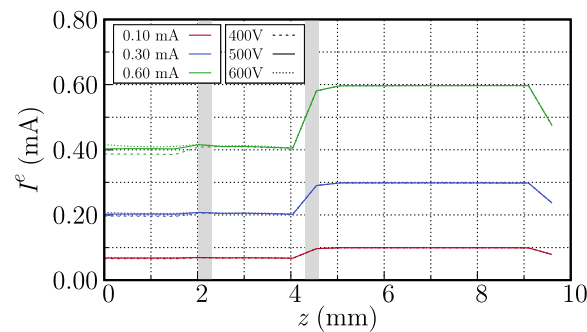
**FIG. 9.** Upstream ( $z=1.0$  mm) electron axial velocity for  $I_{ce} = 0.30$  mA and the acceleration voltages of 400, 500, and 600 V. The electron velocity distribution is extremely uniform in all the domain, meaning that the distribution of kinetic energy in the ionization chamber is quite uniform.

simulations. The upstream ion current ( $I^i \sim 0.1 - 0.65 \mu\text{A}$ ) is always several orders of magnitude smaller than the current of ionizing electrons ( $I^e \sim 0.08 - 0.4$  mA) in the ionization chamber.

The abrupt decrease in  $I^i$  observed in Fig. 10(a) around the axial distance  $z = 2.0$  mm corresponds to the loss of ions captured by the extraction grid. Similarly,  $I^e$  current reduces in Fig. 10(b) along the shadowed area close to  $z = 4.5$  mm as electrons from the cathode are



(a) Ion axial current



(b) Electron axial current

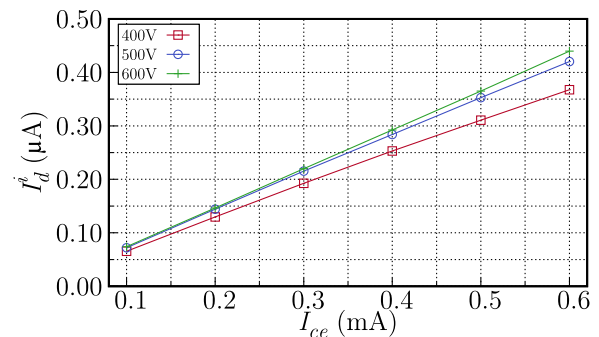
**FIG. 10.** The axial currents of ions (a) and electrons (b) for  $I_{ce} = 0.10, 0.30,$  and  $0.60$  mA, and  $V_{AC} = 400, 500,$  and  $600$  V. Shaded rectangles represent the location of the two grids. The extracted  $\text{Ar}^+$  current is directly affected by the inflow of electrons, and it has also an impact on the flow of electrons and ions, as it modifies the electrical transparency of the system.

lost at the cover grid. Since the holes of both grids are aligned and have the same diameter, reductions in  $I^i$  at the cover grid and of  $I^e$  at the extraction grid are more reduced in both cases.

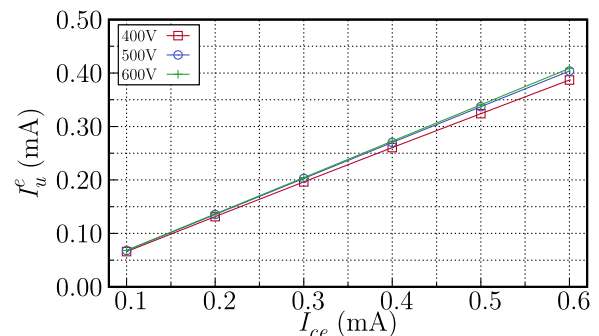
As shown earlier, the acceleration voltage has an impact on both downstream ion and upstream electron currents. Higher  $V_{AC}$  values allow for an additional number of electrons to enter the ionization chamber with higher kinetic energies, thus increasing the  $\text{Ar}^+$  ion production, as shown in Fig. 10(a). The ionizing electron flow  $I_{ce}$  governs the ion production and the exhausted  $\text{Ar}^+$  current increments from  $V_{AC} = 400$  V (dotted line) to  $600$  V (dashed line). Higher acceleration potentials reduce the ions captured at the grids, thus increment the electrical transparency of the system. Figure 10(b) shows the ionizing electron currents at the upstream that also are slightly increased by the  $V_{AC}$  potential as electrons reach the ionization chamber with a higher kinetic energy.

Figure 11 shows the linear dependence between the cathode current  $I_{ce}$  and the axial  $\text{Ar}^+$  downstream  $I_d^i$  ( $z = 7.5$  mm) and electron upstream  $I_u^e$  ( $z = 1.0$  mm) currents for the parameters studied here. The increments in the acceleration potential  $V_{AC}$  give higher slopes in Figs. 11(a) and 11(b). Nevertheless, 500 and 600 V are closer to each other than to the 400 V, which indicates that the effect of  $V_{AC}$  on the currents is non-linear.

Figure 12 characterizes the electric transparency performance of the two-grid system of the *alphie* plasma thruster. The ratio  $I_u^e/I_{ce}$



(a) The  $\text{Ar}^+$  downstream axial current



(b) The electron upstream axial current

**FIG. 11.** The ion downstream current (a) and electron upstream current (b) for  $V_{AC} = 400, 500,$  and  $600$  V in the range of  $I_{ce}$  studied in this work. Both currents depend linearly of the electron cathode current  $I_{ce}$  the slopes increment with the  $V_{AC}$  potential.

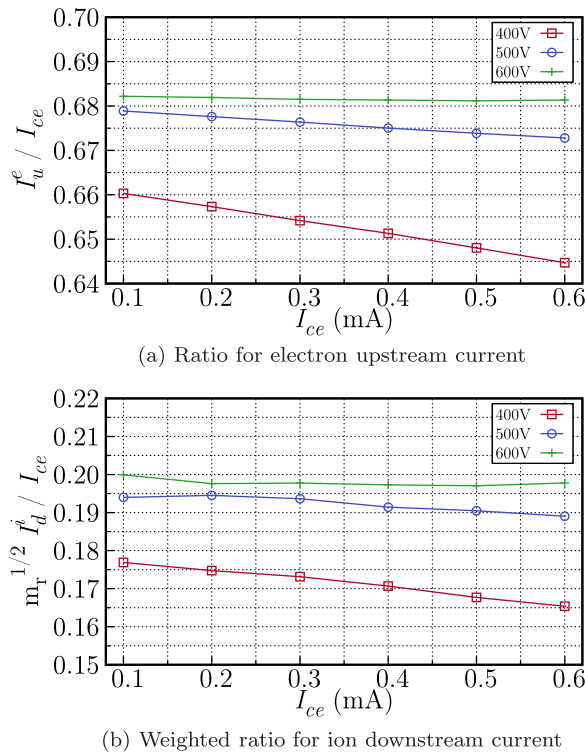


**FIG. 12.** Ratio of electron upstream current (a) and scaled  $\text{Ar}^+$  current (b) as a function of  $I_{ce}$  with respect to the electron current.

means the fraction of electrons that reach the upstream side per input downstream cathode current, and it is represented in Fig. 12(a) as a function of  $I_{ce}$  for the three  $V_{AC}$  voltages studied.

Between 66.5% and 68.5% of electrons provided by the cathode reach the upstream side of Fig. 2 for the  $I_{ce} = 0.1 - 0.6$  mA cathode currents studied. The acceleration voltage has an impact on this ionizing electron transport that slightly decreases with  $I_{ce}$  for the lower voltages.

In Fig. 10(a), the ion currents are orders of magnitude below the  $(0.67 - 0.68) \times I_{ce}$  flow of ionizing electrons that enter the ionization chamber. This means that the number of ionizing collisions is relatively small, and most high-energy electrons are collected at the metallic walls of the ionization chamber, represented by  $I_E$ .

The transport of heavy ions requires a larger number of electrons as Fig. 12(b) shows, where the weighted ratio

$$\sqrt{\frac{m_i}{m_e}} \frac{I_d^i}{I_{ce}} = \sqrt{m_r} \frac{I_d^i}{I_{ce}} \quad (8)$$

for the  $I_d^i$  downstream current of  $\text{Ar}^+$  ions is represented. The acceleration voltage  $V_{AC}$  increases the ion current transported that also slightly decreases with the  $I_{ce}$  cathode current.

The proportionality factor is  $\sqrt{m_r} \sim 240$  for argon, and results in Fig. 12(b) indicate that to sustain the exhausted ion currents of Fig. 10(a) requires a cathode current orders of magnitude higher in the counterflow of charges. The acceleration potential slightly reduces the required electron current that increases with  $I_{ce}$  for the lower voltages.

## VI. CONCLUSIONS

A full particle-in-cell code, named *fpac*, has been used to study the counterflow of charges taking place in the Alternative Low-Power Hybrid Ion Engine (*alphie*). A model has been presented to include the ionization rate of the argon gas employed as propellant, which estimates the collisional charge production in the ionization chamber as a function of the electron current from the external cathode. This model is imposed as the upstream boundary for the electrons coming from the external cathode and passing through the grids' system. Therefore, this model allows self-consistent simulations where the ion current from the ionization chamber is not a boundary condition as in previous works.<sup>16,17</sup> However, some approximations, such as the effective ionization time of electrons in the gas chamber is still required, which will be improved with future numerical simulations.

The model allows simulating the *alphie* plasma thruster using control parameters similar to those employed in the laboratory testing, namely, the input current of electrons from the external cathode  $I_{ce}$  and the acceleration voltage  $V_{AC}$ , which provides the variable throttle capability of this thruster.

The simulations presented here show the distinct dynamic of *alphie* grid system regarding classical GIE. It is found that the two parameters studied here,  $I_{ce}$  and  $V_{AC}$ , have a clear influence on the ion beam exhausted by the *alphie*, which is directly related to the thrust delivered by the system.

An increase in the amount of available electrons downstream of the grid system results in more ionization events, which straightforwardly increases the ion beam current. Additionally, the acceleration voltage has two main effects. First, it increases the electrical transparency of the system, allowing more ions and electrons to pass through. Second, it increases the energy of electrons going toward the ionization chamber, growing the number of ions produced.

Future simulations will improve on the definition of the ionization boundary and will try to optimize the grid system to increase both the inflow of high-energy electrons and the outflow of heavy ions to provide thrust. Additionally, simulations, including the cathode placed downstream the grid system, and multiple holes should be carried out to study the flow of electrons and the current reaching the ionization chamber in detail.

## AUTHOR DECLARATIONS

### Conflict of Interest

The authors have no conflicts to disclose.

### Author Contributions

**J. Gonzalez:** Conceptualization (equal); Data curation (equal); Formal analysis (equal); Funding acquisition (equal); Investigation (equal); Methodology (equal); Project administration (equal); Resources (equal); Software (equal); Supervision (equal); Validation (equal); Visualization (equal); Writing – original draft (equal); Writing – review & editing (equal). **L. Conde:** Conceptualization (equal); Data curation (equal); Formal analysis (equal); Funding acquisition (equal); Investigation (equal); Methodology (equal); Project administration (equal); Resources (equal); Software (equal); Supervision (equal); Validation (equal); Visualization (equal); Writing – original draft (equal); Writing – review & editing (equal). **J. M. Donoso:** Conceptualization (equal); Data curation (equal); Formal analysis (equal); Funding acquisition (equal); Investigation (equal); Methodology

(equal); Project administration (equal); Resources (equal); Software (equal); Supervision (equal); Validation (equal); Visualization (equal); Writing – original draft (equal); Writing – review & editing (equal).

## DATA AVAILABILITY

The data that support the findings of this study are openly available in Zenodo, at <https://zenodo.org/record/8358561>, Ref. 33.

## REFERENCES

- <sup>1</sup>D. M. Goebel and I. Katz, *Fundamentals of Electric Propulsion. Ion and Hall Thrusters* (John Wiley & Sons, Hoboken, NJ, 2008).
- <sup>2</sup>S. Mazouffre, *Plasma Source Sci. Technol.* **25**, 033002 (2016).
- <sup>3</sup>I. Levchenko, S. Xu, S. Mazouffre, D. Lev, D. Pedrini, D. Goebel, L. Garrigues, F. Taccogna, and K. Bazaka, *Phys. Plasmas* **27**, 020601 (2020).
- <sup>4</sup>S. T. Kosonen, T. Kalvas, V. Toivanen, O. Tarvainen, and D. Faircloth, *Plasma Source Sci. Technol.* **32**, 075005 (2023).
- <sup>5</sup>M. Sangregorio, X. K. N. Wang, N. Guo, and Z. Zhang, *Chin. J. Aeronaut.* **31**, 1635 (2018).
- <sup>6</sup>N. Koch, M. Schirra, S. Weis, A. Lazurenko, B. van Reijen, J. Haderspeck, A. Genovese, P. Holtmann, R. Schneider, K. Matyash *et al.*, “The HEMPT concept—a survey on theoretical considerations and experimental evidences,” in *Proceedings of the 32nd International Electric Propulsion Conference (IEPC, Wiesbaden, Germany, 2011)*, Paper No. 2011-236.
- <sup>7</sup>G. Kornfeld, N. Koch, and H.-P. Harmann, “Physics and evolution of HEMP-thrusters,” in *Proceedings of the 30th International Electric Propulsion Conference (IEPC, Florence, Italy, 2007)*, Paper No. 2007-108.
- <sup>8</sup>L. Conde, P. Maldonado, J. Damba, J. Gonzalez, J. Domenech-Garret, J. Donoso, and M. Castillo, *J. Appl. Phys.* **131**, 023302 (2022).
- <sup>9</sup>L. Conde, J. Gonzalez, J. M. Donoso, J. L. Domenech-Garret, and M. A. Castillo, *J. Electr. Propul.* **1**(1), 24 (2022).
- <sup>10</sup>K. Holste, P. Dietz, S. Scharmann, K. Keil, T. Henning, D. Zschätzsch, M. Reitemeyer, B. Nauschütt, F. Kiefer, F. Kunze *et al.*, *Rev. Sci. Instrum.* **91**, 061101 (2020).
- <sup>11</sup>F. Elliott, J. Foster, and M. Patterson, “An overview of the high power electric propulsion (HiPEP) project,” AIAA Paper No. 2004-3453, 2004.
- <sup>12</sup>K. Hara, *Plasma Source Sci. Technol.* **28**, 044001 (2019).
- <sup>13</sup>L. Wei, C. Guobiao, Z. Jinrui, X. Guangqing, and W. Weizong, *J. Phys. D: Appl. Phys.* **54**, 445202 (2021).
- <sup>14</sup>L. Wei, W. Weizong, L. Yifei, and X. Shuwen, *Plasma Source Sci. Technol.* **32**, 085005 (2023).
- <sup>15</sup>T. Brandt, R. Schneider, J. Duras, D. Kahnfeld, F. G. Hey, H. Kersten, F. Jansen, and C. Braxmaier, *Trans. Jpn. Soc. Aeronaut. Space Sci., Aerosp. Technol. Jpn.* **14**, Pb\_235 (2016).
- <sup>16</sup>J. Gonzalez and L. Conde, *Phys. Plasmas* **26**, 043505 (2019).
- <sup>17</sup>D. Dyubo, J. Gonzalez, O. Tsybin, and L. Conde, “Optimizing of ALPHIE grid system with particle-in-cell simulations,” in *International Youth Conference on Electronics, Telecommunications and Information Technologies* (Springer, 2022), Vol. 268, pp. 271–280.
- <sup>18</sup>L. Conde, J. Domenech-Garret, J. Donoso, J. Damba, S. Tierno, E. Alamillo-Gamboia, and M. Castillo, *Phys. Plasmas* **24**, 123514 (2017).
- <sup>19</sup>L. Conde, J. Gonzalez, J. Donoso, J. Domenech-Garret, J. Damba, P. Maldonado, J. Grabulosa, and M. Lahoz, “Physics and performance of the alternative low power hybrid ion engine (ALPHIE) for space propulsion,” in *Proceedings of the 36th International Electric Propulsion Conference (IEPC, Vienna, Austria, 2019)*, Paper No. 2019-A-643.
- <sup>20</sup>H. Li, L. Zhang, S. Zhang, J. Yang, and A. Sun, *Plasma Source Sci. Technol.* **32**, 044002 (2023).
- <sup>21</sup>J. A. Bittencourt, *Fundamentals of Plasma Physics* (Springer Science & Business Media, 2004), Chap. XVIII.
- <sup>22</sup>D. Dyubo, J. Gonzalez, O. Tsybin, and L. Conde, *Phys. Plasmas* **28**, 103509 (2021).
- <sup>23</sup>J. Boris, “Relativistic plasma simulation-optimization of a hybrid code,” in *Proceedings of the 4th Conference in Numerical Simulations of Plasmas* (Naval Res. Lab. Washington, DC, 1970), pp. 3–67.
- <sup>24</sup>G. L. Delzanno and E. Camporeale, *J. Comp. Phys.* **253**, 259 (2013).
- <sup>25</sup>See <https://github.com/OpenMathLib/OpenBLAS/blob/develop/USAGE.md> for OpenBLAS.
- <sup>26</sup>J. Damba, P. Argente, P. Maldonado, A. Cervone, J. Domenech-Garret, and L. Conde, *J. Phys. Conf. Ser.* **958**, 012002 (2018).
- <sup>27</sup>D. Tskhakaya, K. Matyash, R. Schneider, and F. Taccogna, *Contrib. Plasma Phys.* **47**, 563 (2007).
- <sup>28</sup>V. Vahedi and M. Surendra, *Comput. Phys. Commun.* **87**, 179 (1995).
- <sup>29</sup>H. Yajie, X. Guangqing, S. Bin, L. Chang, J. Zhang, and V. A. Saetchnikov, *Chin. J. Aeronaut.* **36**(7), 388–399 (2023).
- <sup>30</sup>S. Biagi, *Nucl. Instrum. Methods Phys. Res., Sect. A* **421**, 234 (1999).
- <sup>31</sup>S. F. Biagi (2004). “Cross sections extracted from program magboltz,” Version 7.1.
- <sup>32</sup>R. Keller, *Nucl. Instrum. Methods Phys. Res., Sect. A* **298**, 247 (1990).
- <sup>33</sup>J. Gonzalez *et al.* (2023). “Self-consistent charge transport model with ionization for the alphie plasma thruster,” Zenodo. <https://zenodo.org/record/8358561>